Medical Image Analysis 46 (2018) 118–129

Contents lists available at ScienceDirect

Medical Image Analysis

journal homepage: www.elsevier.com/locate/media

Cerebrovascular network registration via an efficient attributed graph matching technique

Sepideh Almasi[a,*], Alexandra Lauric[b], Adel Malek[b], Eric L. Miller[a]

[a] Department Electrical and Computer Engineering, Tufts University, Medford, MA, USA
[b] Department Neurosurgery, Tufts University School of Medicine, Boston, MA, USA

ARTICLE INFO

Article history:
Received 4 May 2016
Revised 6 February 2018
Accepted 20 February 2018
Available online 24 February 2018

Keywords:
Vessel registration
Geometrical graph-based models
Graph matching

ABSTRACT

Registration of vascular networks is an indispensable element of prognostic and diagnostic studies that require structural analysis and comparison over time, among different samples, and to a gold standard. However, vascular networks manifest low spatial texture and sparse structural content so that even small variations in their location can make the intensity-based registration inefficient and prone to errors. Motivated by geometrical graph-based models developed in our prior work, we use the shape information in the graph topology sense to enhance the registration performance. An efficient feature-based registration is presented that seeks correspondence of the bifurcations and branches in a graph matching scheme. Since the graph matching is originally posed a NP-hard quadratic assignment problem (QAP) in the literature, we have designed a node signature that incorporates edge correspondences indirectly. This allows removing the quadratic term in the QAP to recast the problem as a linear assignment problem (LAP) to relieve the computational burden. The LAP is efficiently solvable and is scalable to data with graph representation of larger size. The performance is tested and validated using clinical 3-D angiography images of the human cerebrovasculature as well as synthetic datasets. This method proves to be robust in the face of different structural and algorithm's parameters. Quality of inter-subject and multimodal matching of clinical data has also been confirmed.

© 2018 Elsevier B.V. All rights reserved.

1. Introduction

Tubular networks are one of the fundamental structures in biological and medical studies. They are found for example in skeletal structures, nerve fibers, and systems for propagating gases such as intrathoracic airway trees and vascular networks. Among these networks, cerebrovascular networks in particular are the target of major neurobiological and neuroscientific studies (Amin-Hanjani et al., 2015; Agostoni and Longoni, 2015). To assess the state of a disease during diagnosis, monitoring, and treatment processes, it is crucial to match these networks in different images (Metzen et al., 2009). Generally, two vascular networks are geometrically associable by combination of a global or rigid transformation (concerning the overall alignment of the two structures) and morphings between homologous bifurcations and vessels. Morphings are typically local and rather small due to the limited anatomical deformations between samples (Serradell et al., 2015). Pattern analysis of the morphings provides pathological insights where e.g., larger morphings indicate potential or existing abnormalities or diseases (Ingebrigtsen et al., 2004; Lauric et al., 2014). Measuring these quantities calls for developing accurate and efficient registration with minimal intervention.

The problem of vascular network registration presents a number of unique challenges due to their tubularity. These structures do not have enough spatial texture and are structurally sparse in comparison to other organs, thus even small variations in their location deteriorates the precision. Also, their appearance varies largely between patients such that their intensity-based registration is inefficient and prone to errors (Mitrovic et al., 2013; Benseghir et al., 2015). On a different note, it is of great value to design new methods that require the least level of manual interaction with the growth of databases and emergence of new diagnostic and operational technologies.

Building on the effort in Almasi et al. (2015), we consider the novel, graph-based representation for vasculatures capturing both their geometric and topological information in a manner well adapted to tackling the registration difficulties mentioned in the previous paragraph. We exploit the topology as a mean of capturing the pattern of connectivity among branching points, a powerful asset missing in the majority of registration algorithms. In our geometric graph-based model (GGM), nodes represent the struc-

* Corresponding author.
E-mail address: s.almasi@stanford.edu (S. Almasi).

https://doi.org/10.1016/j.media.2018.02.007
1361-8415/© 2018 Elsevier B.V. All rights reserved.

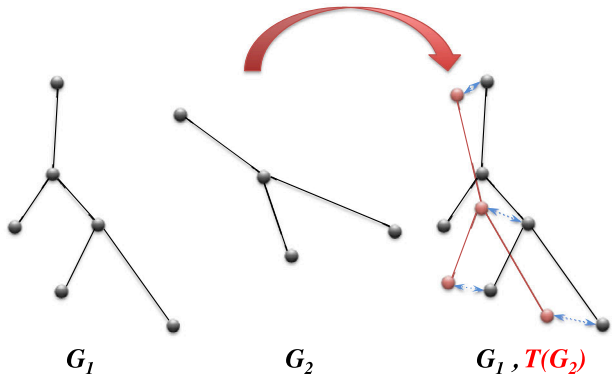


Fig. 1. The rigid transformation T of G_2 that globally aligns it with G_1 and the morphing between nodes of G_1 and $T(G_2)$.

ture's critical points, specially junctions (branching points) and waypoints (points of curvature extrema); while edges model the vessels connecting pairs of neighboring critical points. These models are of great potential advantage in clinical studies as they provide a common representation for physiologically relevant networks allowing for quantitative comparisons to be made across modality, scale, and time. Fig. 1 illustrates how two simplified examples of such model can be registered via the rigid transformation and morphings.

The T denotes the rigid transformation and the blue double-headed arrows show the morphings between the corresponded nodes. Thus, using GGMs and an efficient graph matching technique, we can register the landmarks of vascular networks.

The literature indeed demonstrates that graph matching based registrations usually perform superior to the techniques that only use shape descriptors such as contours (Sebastian and Kimia, 2005; Bai and Latecki, 2008). In recent years, there has been a number of successful efforts toward using graph models to non-rigidly register vasculature. One of the earliest works is Smeets et al. (2010) that registers lung vessel trees by matching bifurcations using their geodesic distances as similarity measure. The matched nodes are found by running a spectral method. This method requires fully connected graphs. The recent work of Serradell et al. (2015) considers a probabilistic model for the nodal distances to match the tree graphs. The approach proposed in (Czajkowska et al., 2015) registers the aorta via matching manually defined points based on the pixel-based intensity features derived from the original grayscale images using the method of (Ma and Latecki, 2012).

The graph matching problem in its original form is defined as an integer quadratic programming (IQP) in which unary and pairwise correspondences are sought between all the nodes (Conte et al., 2004; Burkard, 2013). Joint inclusion of affinity and assignment matrices in the quadratic assignment problem (QAP) yields node and edge correspondences simultaneously (Yan et al., 2015). However, this problem is NP-hard and there is no known polynomial time algorithm to solve it Cho et al. (2010). Thus majority of the state-of-the-art in this area of research has been focused on developing methods that approximate the matching using continuous relaxation of the combinatorial assignment problem (Gold and Rangarajan, 1996; Zaslavskiy et al., 2009) or spectral properties of the adjacency matrices (Leordeanu and Hebert, 2005; Cour et al., 2007; Leordeanu et al., 2012).

The above discussions motivate our development of a novel method that robustly registers GGMs addressing the computational bottleneck. Also, the manual interaction has been significantly reduced via automatic node search in GGMs and calculation of the features. For this purpose, instead of handling the global topological content at once, we present the essence of the data in a feature of lower structural order called the signature. The node signature concept in the context of attributed graph-based data analysis has been used in the following approaches, each of which emphasizes different information of graphs to conduct their analysis. The effort in (Siddiqi et al., 1999) focuses on the hierarchical graphs (trees) and defines the signature as the eigenvalue of the adjacency matrix of each node's sub-tree. The Gori et al. (2005) uses Markov random walk theory to probabilistically compute the node topological signatures. A topology-oriented definition of signature based on the graph traversal notions (breadth first search) is proposed in (Wong et al., 2006). The method proposed in Jouili and Tabbone (2009) poses the signature as a vector incorporating the node degree and weights of the connected edges. The approach of Hu et al. (2013) exploits the graph Laplacians concepts to design the node signatures. A combination of general and local node similarities is considered to serve as signature in Zhu et al. (2013). The general similarity is obtained by spectral analysis where the degree/density in a neighborhood of each node rules the local similarity measure. While useful in their own contexts, none of these methods are quite appropriate for the problem of interest here where the graphs are not, generally, of a tree shape and indeed may be disconnected and where the nature of the raw image data is such that intensity features are not sufficiently reliable for matching purposes.

In this work, we propose a new design of signature that includes local geometrical properties of junctions and vessels in a topology preserving way. For this purpose, we transform GGMs into abstract graphs whose nodes and edges represent the tubular network's bifurcations and branches. The approach we developed is flexible in terms of the specific node and edge attributes, which should be chosen based on the underlying clinical application, used as the basis for matching. Given the application motivating the work here, we consider attributes that are related to the risk of aneurysm formation, growth, and eventual rupture. Recent efforts have shown a correlation between vessel morphology and aneurysmal presence. High curvature of the internal carotid artery was associated with sidewall aneurysm presence (Lauric et al., 2014), whereas wide bifurcation angles were associated with bifurcation aneurysms in middle cerebral artery (Baharoglu et al., 2014) and basilar artery (Tutuncu et al., 2014). Thus, we defined node attributes to be the bifurcations location and edge attributes are approximations of vessels' length and curvature.

As a result of encoding the local connections in an algebraic form, node matching is posed as a Linear Assignment Problem (LAP) yielding an approximate solution in a considerably less computationally expensive manner than the classic QAP method which is NP-hard. We have used a modified version of the graduated assignment (GA) approach that solves the LAP. The reason behind this selection vs. the well-known Hungarian method is that this method accommodates simultaneous null matches for both sets elements. This is crucial for the problem of interest where, depending on the vascular content of the data sets, one must be able to accommodate an arbitrary number of null matches. It is true that the Hungarian method can be adapted to the null match case by building a heavily augmented assignment matrix whose extra columns and rows are zero; however, the added computational complexity of solving this artificially inflated assignment problem can be prohibitive.

The performance of this method is validated using clinical data obtained from magnetic resonance angiography (MRA) and 3D rotational angiography (3DRA) of healthy and diseased human cerebrovasculature and synthetic datasets. The MRA images include vasculature across the entire brain whereas the 3DRA images show vasculature of either right or left hemisphere in a more exhaustive manner. Synthetic data are derived from clinical data through

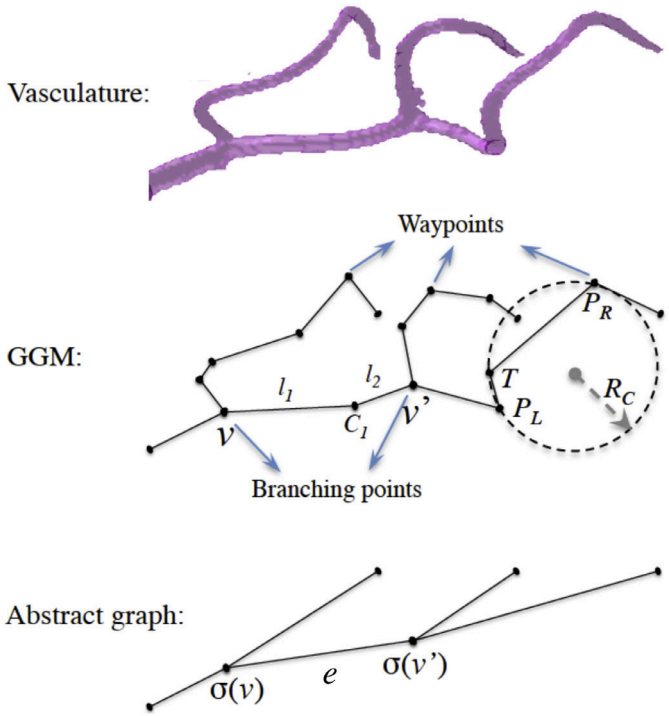


Fig. 2. Top to bottom: Part of a vasculature, its geometrical graph-based model, and attributed abstract graph.

node removal and displacement. We have controlled the parameters contributing to these operations to evaluate the method vs. different structural inclusiveness and deformation levels. Quantitative results in sensitivity and precision calculated for nodes and edges show the method's high reliability in the face of the challenges. Accuracy of the matching algorithm is validated against the state-of-the-art methods. Effectiveness of our method has also been tested for inter-subject cases where graphs are obtained from clinical data of different patients. Both qualitative and quantitative results confirm strong performance of the method in this regard. Finally, data of MRA and 3DRA modalities have been matched through the proposed method to assess its performance for scenarios where only partial structural homogeneities exists.

This paper is organized with Section 2 describing the attributed graph registration problem and the technical details of the proposed approach that seeks the optimized matchings. In Section 3, we describe the evaluation results obtained from synthetic and clinical data. Finally, Section 4 concludes the paper and indicates the possible future paths for continuing this study.

2. Methodology

In this section, we first present relevant definitions and then formulate the matching problem.

2.1. Attributed graph generation

The GGM as proposed in Almasi et al. (2015) and shown in Fig. 2, is a piece-wise linear approximation of the vascular network skeleton that best fits its curvy shape. In this model, edges represent vessel sections that connect pairs of critical points: branching points (bifurcations) or waypoints (points of curvature extrema). Given a GGMs, its general attributed abstract form, $G = (V, E, \phi, \zeta)$, is defined as follows. The G is characterized by a node set V representing vascular bifurcations and endpoints with cardinality $n = |V|$ and edge set $E \subset V \times V$ representing vessel branches that connect the bifurcations and endpoints. Fig. 2 shows an abstract model in the bottom part. The node attribute is its Cartesian coordinates presented by vector $\phi : V \to \mathbb{R}^3$ such that $\phi(v) = [x\, y\, z]^T$. Edge attributes are given by vector $\zeta : E \to \mathbb{R}^2$ such that the first element of $\zeta(v_i, v_j)$ is an estimate of the vessel branch length connecting the v_i and v_j. This measure is obtained by summing the length of all edges in GGM that associate with the abstract edge; *e.g.*, in Fig. 2, the length of e equals $l_1 + l_2$. The second edge attribute is associated with the smoothed curvature of vessels. Local curvatures can be estimated at each waypoint from the angular difference between successive linear segments (Salmon et al., 2006). Given the notations in Fig. 2, the absolute curvature at waypoint T is $C(T) = \frac{1}{R_C(T)}$ where $R_C(T)$ is the radius of the circumcircle of the triangle made by T and its neighboring critical points P_R and P_L:

$$R_C(T) = \frac{s_1\, s_2\, s_3}{\sqrt{(s_1 + s_2 + s_3)(s_1 - s_2 + s_3)(s_1 + s_2 - s_3)(-s_1 + s_2 + s_3)}} \tag{1}$$

where $s_1 = \|\overrightarrow{TP_R}\|$, $s_2 = \|\overrightarrow{TP_L}\|$, and $s_3 = \|\overrightarrow{P_R P_L}\|$.

We define the smoothed curvature to be the summation of the Cs calculated for all the waypoints along an edge.

The graphs of interest in this work are of the non-tree 3-regular form. Therefore, all nodes other than the leaves have exactly three connections (a parent and two child nodes). Utilizing these specifications, we developed a novel node signature feature that simultaneously incorporates the geometrical and topological information of the graphs. The signature of the i^{th} node is defined as

$$\sigma(v_i) = \begin{bmatrix} \phi(v_i) & \phi(v_{i,1}) & \phi(v_{i,2}) & \phi(v_{i,3}) \\ \zeta(v_i, v_i) & \zeta(v_i, v_{i,1}) & \zeta(v_i, v_{i,2}) & \zeta(v_i, v_{i,3}) \end{bmatrix} \in \mathbb{R}^{5\times 4} \tag{2}$$

where $v_{i,1}$, $v_{i,2}$, and $v_{i,3}$ are the three nodes in the first round breadth-first search from v_i. Since these graphs do not have buckles, $\zeta(v_i, v_i) = 0, \forall i$. This design of signature yields the geometrical attributes of interest.

2.2. Graph-based model registration (GMR)

The graph matching problem in its original form is a QAP defined as

$$\hat{A} = arg\,min \sum_{i=1}^{n_1}\sum_{j=1}^{n_2} c_{ij}a_{ij} + \sum_{i=1}^{n_1}\sum_{j=1}^{n_2}\sum_{i'=1}^{n_1}\sum_{j'=1}^{n_2} d_{iji'j'}a_{ij}a_{i'j'},$$
$$a_{ij} \in \{0, 1\} \tag{3}$$

where the a_{ij}s are binary assignment indices forming the assignment matrix A for which each row's and each column's summation cannot exceed one. The $a_{ij} = 1$ indicates that $v_i \in V_1$ and $v_j \in V_2$ are matched. The c_{ij} is the cost of assigning v_i to v_j where $d_{iji'j'}$ quantifies the similarity between edges (v_i, v_i') and (v_j, v_j'). Solving this quadratic combinatorial problem is NP-hard.

By proposing the node signature that incorporates the edge correspondences indirectly, we allow for removing the quadratic term from (3) to recast this QAP as a LAP that approximates the graph matching problem with considerably lower computational complexity and high precision. The goal is to maximize the similarity of matching nodes' signatures across two given attributed abstract graphs that guarantees the local consistency of edge matchings in place of the quadratic term. Therefore, we propose c_{ij} to be function of Euclidean distance of the signatures.

After global alignment of graphs using the RANSAC based method of Sonka et al. (2014) provided for aligning the training shapes, we defined a node's signatures by concatenating the attribute vectors of its connection in an arbitrary fashion. Thus, it is generally the case that we need to permute the columns of

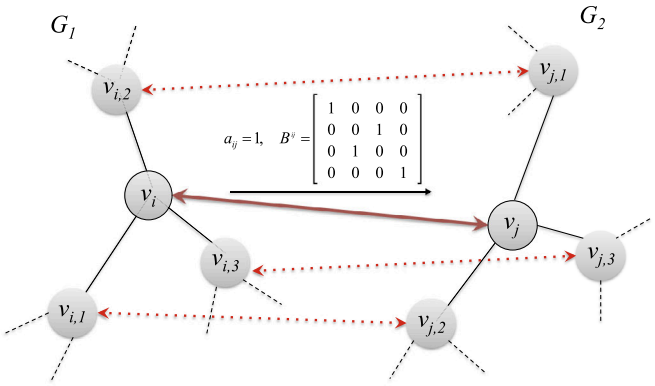


Fig. 3. The B^{ij} permutes $\{v_{i,1}, v_{i,2}, v_{i,3}\}$ so that $\|\sigma(v_j) - B^{ij}\sigma(v_i)\|_F$ is minimized. (For interpretation of the references to color in this figure, the reader is referred to the web version of this article.)

signatures such that attributes of the connections of a node will be compared to the attributes of the more similar connections of the other node. Fig. 3 shows one matching example between v_i and v_j. In this example, the desired correspondences are shown with double headed red arrows. When solving the LAP, the true c_{ij} has to be the difference between attributes of these corresponded nodes. This calls for multiplying $\sigma(v_i)$ by the given B^{ij} such that $\sigma(v_i)B^{ij}$ will be minimally distant from $\sigma(v_j)$ in Frobenius norm sense. This example demonstrates the need for 4×4 permutation matrices $B^{ij}, i = 1\ldots, n_1, j = 1\ldots, n_2$ in assignment cost definition. We set $B^{ij}_{11} \equiv 1$ where B^{ij}_{mn} refers to the element of B^{ij} on row m and column n. The reason for this assignment is that base nodes are put at the beginning of signatures by definition. The B^{ij}s are determined by Hungarian method for all pairs of nodes across the two graphs.

Given the above definitions and labeled globally aligned graphs G_1 and G_2, matching problem is defined as

$$\hat{A} = arg\,min \sum_{i=1}^{n_1}\sum_{j=1}^{n_2} a_{ij}\left(\|\sigma(v_j) - \sigma(v_i)\hat{B}^{i,j}\|_F - \lambda\right)$$
$$a_{ik} \in \{0,1\}, \quad \sum_{i=1}^{n_1} a_{ik} \le 1, \text{ and } \sum_{j=1}^{n_2} a_{kj} \le 1, \ \forall k \tag{4}$$

where the first term guarantees the data and structure fidelity, and the second/regularization term gives rise to a higher number of assignments. By the sub-graph isomorphism problem definition, an assignment matrix can only take at most one non-zero element in each row or column to guarantee that every node of one graph is assigned to at most one node in the other graph (Chui and Rangarajan, 2003). The inequality in the above constraints allows for points to remain unmatched. In absence of the second term, the optimization delivers all-zero matrices meaning that none of the nodes get matched due to the non-negative assignment costs and allocation for null matches ($\sum_{i=1}^{n_1} a_{ik} \le 1, \forall k$ and $\sum_{j=1}^{n_2} a_{lj} \le 1, \forall l$). The parameter λ controls the assignment rate and is tuned in a manner that reflects the expected magnitude of the first term; i.e, nominal distances separating homologous bifurcations in a pair of graphs. In other words, λ is the threshold level on assignment costs that prevents node pairs with less likely anatomical correspondences in the solution.

Considering the higher accuracy of continuous relaxation techniques (Cho et al., 2010) compared to the state-of-the-art techniques such as SM (Leordeanu and Hebert, 2005), SMAC (Cour et al., 2007), IPFP (Leordeanu et al. 2009), HGM (Zass and Shashua., 2008), and linear programming (Leordeanu and Hebert, 2005), we solve the problem (4) by an approach adapted

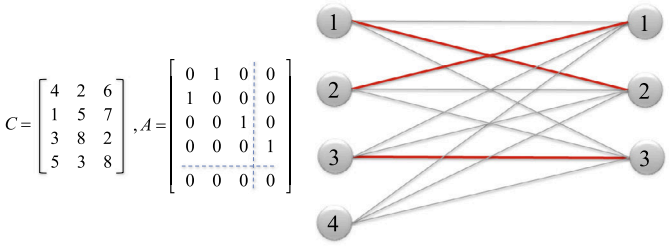


Fig. 4. The red links are the optimal node assignments given the cost matrix C. (For interpretation of the references to color in this figure legend, the reader is referred to the web version of this article.)

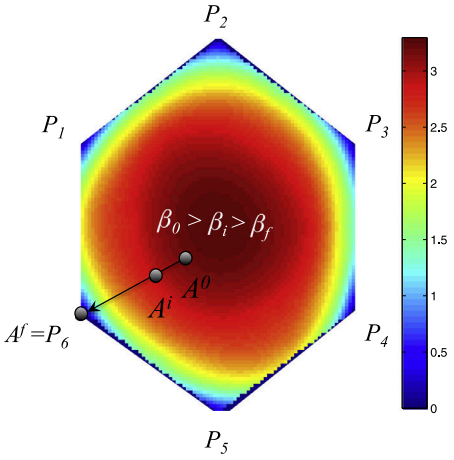


Fig. 5. Figurative description of annealing process: The assignment matrix starts from regions of higher entropy depicted by warmer colors and moves toward one of the polytope corners (P_6 here) as β decreases.

from GA method (Gold and Rangarajan, 1996; Gold et al., 1998). This choice of algorithm is validated in Section 3.5.

The approach starts with relaxing the a_{ij}s to the [0, 1] interval to avoid trapping in the local minima, a common challenge of combinatorial problems, by allowing partial/soft matches between points and smooth updates during the optimization. Then, A is augmented with a slack row and column for indexing unmatched nodes as shown in the example of Fig. 4.

In this Figure, C is the assignment cost matrix. When $v_i \in V_1$ does not match with any of the nodes in V_2, $a_{i,n_2+1} = 1$. For the non-matched $v_j \in V_2$, $a_{n_1+1,j} = 1$. Given the updated definition of A, the assignment constraints are

$$\sum_{i=1}^{n_1+1} a_{ik} = 1, \ k = 1,\ldots,n_2, \quad \sum_{j=1}^{n_2+1} a_{lj} = 1, \ l = 1,\ldots,n_1. \tag{5}$$

These constraints imply a slightly relaxed form of doubly stochasticity for A that means every row and column sums to one. Doubly stochastic matrices in general are convex hulls of permutation matrices of the same size (Horn and Johnson, 2012). Fig. 5 schematically demonstrates a hexagon area representing the matrices of size 6×6 that is convex hull of the six permutation matrices of the same size, $P_i, i = 1\ldots, 6$. Interestingly, the entropy of matrices, $-\sum_{i=1}^{n_1}\sum_{j=1}^{n_2} a_{ij}\log(a_{ij})$, falling in this region changes in a particular pattern. Warmer colors in the center of Fig. 5 represent matrices of higher entropy with more randomly distributed elements. The binary matrices at the corners have the lowest level of entropy.

The GA uses this property to achieve the binaryness by gradually transitioning the result over the continuous space to the corners. Via combination of continuous relaxation, entropy controlling, and doubly stochasticity, we approximate the problem

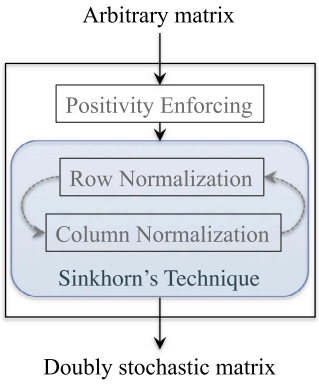


Fig. 6. Softassign method that turns any matrix into its doubly stochastic version.

(4) with

$$\hat{A} = argmin \sum_{i=1}^{n_1}\sum_{j=1}^{n_2} a_{ij}\|\sigma(v_j) - \sigma(v_i)\hat{B}^{ij}\|_F - \lambda a_{ij} + \beta a_{ij}\log(a_{ij}).$$

$$a_{ij} \in [0,1], \quad \sum_{i=1}^{n_1} a_{ik} \le 1, \text{ and } \sum_{j=1}^{n_2} a_{kj} \le 1, \ \forall k \tag{6}$$

In this optimization problem, β controls the entropy level of the solution; smaller β leads the A to having lower entropy and its entries will converge to either 0 or 1. Thus, binary matrices are achieved by smooth reduction of β (Gold and Rangarajan, 1996). This process is called annealing and β is the annealing rate. This rate is controlled by β_r that balances between convergence and robustness. In such recursive manner, the optimal matrix obtained at each β level, is used to initialize the next stage. The annealing stops when β reaches β_f which is set by the average of the squared distance between the signature of the nearest neighbors in datasets.

To ensure the doubly stochasticity of A, the soft assign method (Rangarajan et al., 1997) is used. Fig. 6 shows the essence of this technique that includes positivity enforcement and Sinkhorn's technique (Sinkhorn, 1964) where the later is consecutive row and column normalizations.

Prior to the start of process and at lines 1 of Algorithm 1, a_{ij}s are initialized as $a_{ij} = 0$ and $\beta = \beta_0$. In the next step, $\hat{B}^{ij}$s are set by running the minimum weight Hungarian assignment between columns of $\sigma(v_i)$ and $\sigma(v_j)$ where weights are $\|\phi(v_{j,k}) - \phi(v_{i,l})\|_F$, $k,l = 2,\ldots,4$, $\forall i,j$. The assignment costs are then calculated as

$$Q_{ij}^A = \|\sigma(v_j) - \sigma(v_i)\hat{B}^{ij}\|_F - \lambda. \tag{7}$$

Positivity is enforced on a_{ij}s with exponentiation such that

$$a_{ij}^l = \exp(\beta a_{ij}^{l-1} Q_{ij}^A). \tag{8}$$

The constraints in (5) are enforced by iteratively normalizing the rows and columns except for the slack variables ($a_{n_1+1\,j}$ and $a_{i\,n_2+1}, \forall i,j$) until A converges or the number of iterations, I, exceeds $I_{\max}$:

$$a_{ij} = \frac{a_{ij}}{\sum_{j=1}^{n_2+1} a_{ij}}, \quad i = 1,\ldots,n_1$$

$$a_{ij} = \frac{a_{ij}}{\sum_{i=1}^{n_1+1} a_{ij}}, \quad j = 1,\ldots,n_2. \tag{9}$$

where the convergence criterion is

$$\frac{1}{n_1 \times n_2}\sum_{i=1}^{n_1}\sum_{j=1}^{n_2} |a_{ij}^l - a_{ij}^{l-1}| < \epsilon. \tag{10}$$

Algorithm 1 Node matching algorithm

Inputs: G_1, G_2, β_0, $\beta_r < 1$, β_f, I_{max}, λ, and ϵ
Initialization:
1: $a_{ij}^0 \leftarrow 0, \quad i = 1,\ldots,n_1+1, \ j = 1,\ldots,n_2+1$
2: $\beta = \beta_0$
3: **Calculation:** Signatures $\forall v_i \in G_1, v_j \in G_2$.
4: $\hat{B}^{ij} \leftarrow$ Assignment matrix for columns of $\sigma(v_i)$ to columns of $\sigma(v_j)$ obtained by Hungarian method $\forall i,j$.
5: $Q_{ij}^A \leftarrow \|\sigma(v_j) - \sigma(v_i)\hat{B}^{ij}\|_F - \lambda$
6: **while** $\beta \ge \beta_f$ **do**
7: $I \leftarrow 1$
8: Positivity enforcement: $a_{ij}^l \leftarrow \exp(\beta a_{ij}^{l-1} Q_{ij}^A)$.
9: **while** $\|a^l - a^{l-1}\|_F > \epsilon$ or $I < I_{max}$ **do**
10: $a_{ij}^{l+1} = \frac{a_{ij}^l}{\sum_{j=1}^{n_2+1} a_{ij}^l}, \quad i = 1,\ldots,n_1$
11: $a_{ij}^{l+1} = \frac{a_{ij}^l}{\sum_{i=1}^{n_1+1} a_{ij}^l}, \quad j = 1,\ldots,n_2$
12: $a_{ij}^l \leftarrow a_{ij}$
13: $I \leftarrow I+1$
14: **end**
15: $a_{ij}^0 \leftarrow a_{ij}^l \quad \forall i,j$
16: Anneal: $\beta \leftarrow \beta_r\beta$
17: **end**
18: $A = a_{ij}^l$
19: **Binarization:** A
Output: A

These steps are repeated for each β until reaching β_f. Matrices are then fully binarized through maximum element filtering: in each row, the maximum valued element is turned into one and the rest of the elements are set to zero, $a_{ij} = 1$ if $a_{ij} \ge a_{ik}, k = 1,\ldots,n_2+1$. Edges are matched subsequently using the following definition.

Definition 1. Suppose attributed graphs $G_1 = (V_1, E_1, \phi_1, \zeta_1)$ and $G_2 = (V_2, E_2, \phi_2, \zeta_2)$ are corresponded with A. Let v_i, $v_k \in V_1$ and v_j, $v_l \in V_2$. The $(v_i, v_k) \in E_1$ and $(v_j, v_l) \in E_2$ are said to be matched if $a_{ij} = a_{kl} = 1$.

3. Experiments

In this section, we demonstrate how the proposed registration method performs using synthetic and clinical data. The provided results validate its reliability under the influence of perturbation factors such as node displacement and unmatched nodes count.

3.1. Clinical data

We used nine MRA and twelve 3DRA images from the human brain vasculature for this study. Two examples are shown in Figs. 7(a,b) respectively. Data was randomly selected from a prospectively maintained database. Among the 3DRA datasets, five are gathered from healthy patients and seven are obtained from patients with aneurysm in arbitrary locations of the cerebrovasculature. Patients underwent either 3D catheter-based cerebral angiography, with angiograms acquired using a Siemens Artis calibrated biplane system, or 3T MRA of the brain, with images acquired using a 3T Achieva unit (Philips Healthcare). Volume reconstructions were performed using the available clinical software packages, to yield a 3D volumetric dataset. The size of each MRA volume was $512 \times 512 \times 250$ voxels with $0.39 \times 0.39 \times 0.5$ mm voxel size. The size of each 3DRA volume was $512 \times 512 \times 395$ voxels with 0.279 mm isotropic resolution.

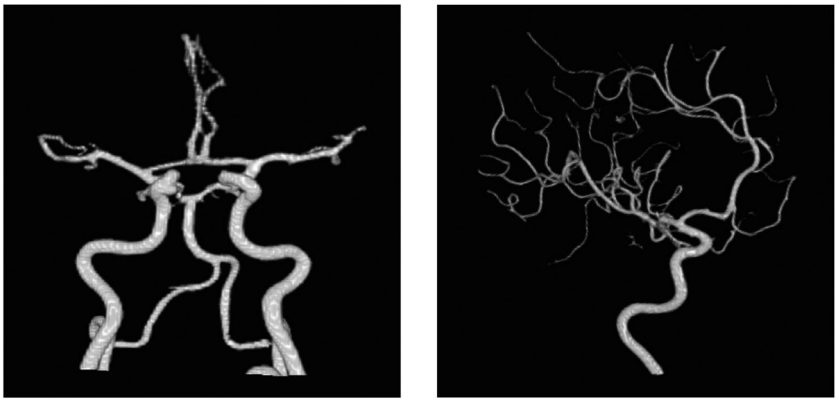


Fig. 7. (a) MRA and (b) 3DRA images of the cerebrovasculature.



Fig. 8. Left to right: A segmented 3DRA dataset, its GGM, and the abstract graph.

The cerebral blood vessels are segmented using the level-set algorithm based on open-source Insight Segmentation and Registration Toolkit (ITK) (version 3.20) libraries. The graph-based models are then generated by means of Almasi et al. (2015). Attributed graph models are then formed by following the procedure described in Section 2.1. Fig. 8 shows the products of these steps for a 3DRA dataset.

3.2. Synthetic data

Synthetic graphs are derived from the attributed graphs of the clinical data which, going forward, we refer to as *base graphs* in a manner that closely simulates the natural structural variations. For this purpose, we define a node level, L, as one plus its distance to the circle of willis (CoW) such that nodes on the CoW are at level $L = 1$. The nodes at higher levels, farther from CoW, receive higher chance of perturbations such as deletion and displacement as they correspond with smaller and less well resolved vessels that are more prone to processing errors. They also vary more among the patients. The perturbations are simulated by a non-linear transformation $\mathcal{T}$ defined as

$$w_j = \mathcal{T}(v_i) = \begin{cases} v_i + \eta & \text{with probability } \alpha\, e^{(\alpha-1)(L-1)} \\ \varnothing & \text{with probability } 1 - \alpha e^{(\alpha-1)(L-1)}. \end{cases} \tag{11}$$

The parameter $\alpha \in [0, 1]$ affects the percentage of remained nodes in the synthetic data that implies the graph size. Fig. 9 shows a plot of node preservation probability vs. α and L. Larger αs yield synthetic graphs with higher node counts where the exponential dependency of the probability on L yields a gradual and less random node deletion that fits better to the real data models; nodes at higher levels from CoW receive a higher removal probability. Structural deformations in the form of node displacement are produced by adding Gaussian noise $\eta \sim \mathcal{N}(0, \sigma_\eta^2)$ to the Cartesian coordinate of nodes. The edge perturbations are imple-

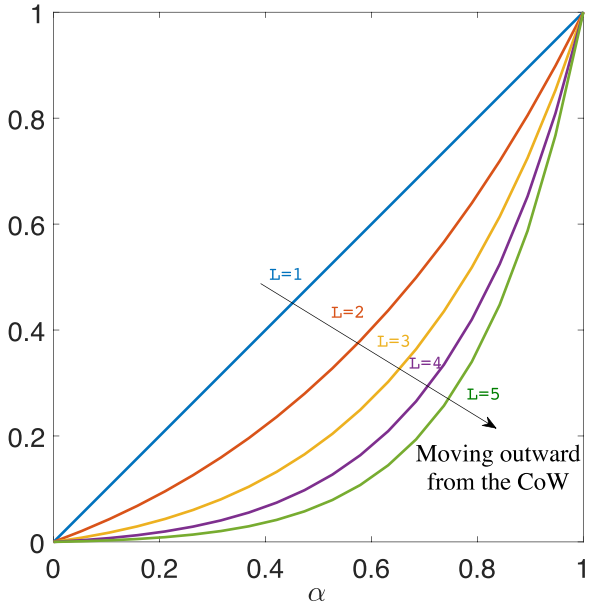


Fig. 9. Probability of a node to remain in the synthetic graph vs. α as a function of its level L from CoW.

Table 1
Performance measures versus problem size (α).

α	*TPR* (node/edge)	*PPV* (node/edge)	*FPR* (node/edge)
0.7	0.94/0.91	0.96/0.95	0.03/0.04
0.5	0.91/0.88	0.94/0.92	0.05/0.05
0.4	0.90/0.86	0.90/0.90	0.05/0.06
0.2	0.87/0.86	0.87/0.89	0.06/0.08
0.1	0.80/0.82	0.83/0.84	0.08/0.09

Table 2
Performance measures versus structural deformation level (σ_η).

σ_η	*TPR* (node/edge)	*PPV* (node/edge)	*FPR* (node/edge)
5	0.92/0.90	0.95/0.93	0.04/0.05
10	0.86/0.83	0.91/0.88	0.06/0.08
15	0.84/0.78	0.87/0.86	0.09/0.11
20	0.71/0.65	0.80/0.78	0.10/0.13
25	0.63/0.56	0.75/0.71	0.12/0.16

Table 3
Performance measures versus the regularization parameter (λ).

λ	*TPR* (node/edge)	*PPV* (node/edge)	*FPR* (node/edge)
10	0.94/0.91	0.95/0.94	0.03/0.06
50	0.93/0.92	0.98/0.96	0.04/0.08
100	0.81/0.74	0.98/0.91	0.06/0.09
150	0.76/0.68	0.90/0.82	0.07/0.09
200	0.72/0.66	0.87/0.82	0.09/0.10

mented using the formulation (11) omitting the displacement parameter, η. Throughout experiments, the base graph is considered as the ground truth and its synthetic variations are utilized to test the method against the problem size and deformation factors controlled by α and σ_η.

3.3. Parameter tuning

The GA has been shown to converge and provide satisfactory results given well-tuned parameters (Schellewald et al., 2007). For all of the experiments in this work, β_0, β_r, and β_f are set as suggested by Chui and Rangarajan (2003). The β_0 is set to the largest square distance of all signature pairs trained by the ground truth. The annealing rate that balances between convergence rate and robustness has to be a value between 0.9 and 0.99. Here, we let $\beta_r = 0.95$. The $\beta_f = 0.01$, $I_{\max} = 30$, and $\epsilon = 0.01$.

3.4. Validation metrics

The accuracy is measured in terms of sensitivity, precision, and false positive rate (*FPR*) for matched nodes and edges. Measurements are reported in Tables 1–3 and a receiver operating characteristic (ROC) curve. Sensitivity or true positive rate (*TPR*) equals the ratio of correctly detected matches to the total number of truly corresponding features. Precision or positive predictive value (*PPV*) is defined by the ratio of correctly detected to the total number of matched features. The *FPR* equal 1-specificity.

3.5. Performance evaluation

As mentioned in Section 2.2, prior to every matching procedure, the graphs are rigidly and roughly brought to the same alignment using the method provided in Sonka et al. (2014).

3.5.1. Synthetic data

The key component in developing a graph matching technique for real data is robustness; its performance has to be minimally impacted by reasonable geometrical distortions and presence of unmatched features. This is assessed by exploring performance as a function of those parameters impacting graph structure including the problem size (α), spatial deformation (σ_η), and optimization accuracy (λ). Fig. 10 shows a base abstract graph and its three synthetic modifications in each of which one of the parameters has changed. The synthetic graph of Fig. 10(b) is affected by node loss where $\alpha = 0.18, \sigma_\eta = 0$ and $\lambda = 10$. Fig. 10(c) shows a graph with perturbed nodal locations obtained by setting $\alpha = 0, \sigma_\eta = 10$, and $\lambda = 10$. The last synthetic graph is designed to test the effect of regularization parameter λ. For this reason, parameters are set as $\alpha = 0, \sigma_\eta = 5$, and $\lambda = 50$. In the synthetic graphs, nodes have double labels. The label on the right side shows the matched node in the base graph where the left side label shows the ground truth. The right side label is replaced with a cross sign for the unmatched nodes. Edges are color-coded for visual appreciation of the matching results where matched edges received similar colors. Non-matched edges are shown in black.

The effect of α on performance is investigated on a collection of synthetic datasets that are obtained from ten base graphs (5 from MRA and 5 from 3DRA data). The synthetic graphs are generated using a range of α from 0.7 to 0.1 with decrements of 0.1 while σ_η is set with 5 and $\lambda = 100$. Synthetic graphs are matched to each other and the base graphs. Averaged *TPR*, *PPV*, and *FPR* for eighty resulting graphs are presented in Table 1.

The node related *TPR* shows a positive correlation with size. This behavior can be interpreted with the following argument. As α falls, the node density reduces and fewer structure remains to be matched. Thus, nodes are matched with less sensitivity (*TPR* decreases). The edge related sensitivity also demonstrates a decreasing trend as more nodes are missed. The precision decreases for node detection reflecting the increased power of method in capturing correspondences as the problem size increases and more structure is present. In general, the method shows a robust behavior against the structural loss where the *TPR* and *PPV* decrease by less than 12% where the number of missed nodes increases by 200%. This implies that the registration method has a low dependency on the quality of preprocessing steps. The mean *FPR* is 0.05 for nodes and 0.06 for edges. This also confirms that the node and edge matchings are less sensitive to this factors from the false positive matching outlook.

Evaluations regarding the deformation tolerance are carried out by varying σ_η over five levels uniformly spaced from 5 to 25 for the same base graphs as mentioned above. The reason for selection of these variance levels stems from the fact that the minimum distance between neighboring bifurcations in all datasets is greater than ten voxels. For $\alpha = 0.1$ and $\lambda = 100$, averaged performance measures are given in Table 2. According to these results, the sensitivity and precision decrease with larger displacements. The displacements cause higher number of false alarms and lower number of true negative detections that leads to the lower *TPR* and *PPV* rates while having rather higher *FPR*s.

Next, we present the experimental results that show the effect of regularization parameter on the performance. Synthetic graphs are built similar to the other two cases described above having $\alpha = 0.1$ and $\sigma_\eta = 5$. Given the results obtained from λ values ranging from 10 to 200, performance metrics are calculated and provided in Table 3. Results show that setting the λ requires some care. Small values of λ greatly limit the matching range. On the other hand, the matching becomes too flexible at large values of λ giving rise to false matchings. For the rest of evaluations, λ is set with 50 that based on the content of Table 3 yields satisfactory sensitivity and precision.

3.5.2. Clinical data

Inter-subject matching: Here, we explore the method's performance across different subjects thereby allowing for the evaluation

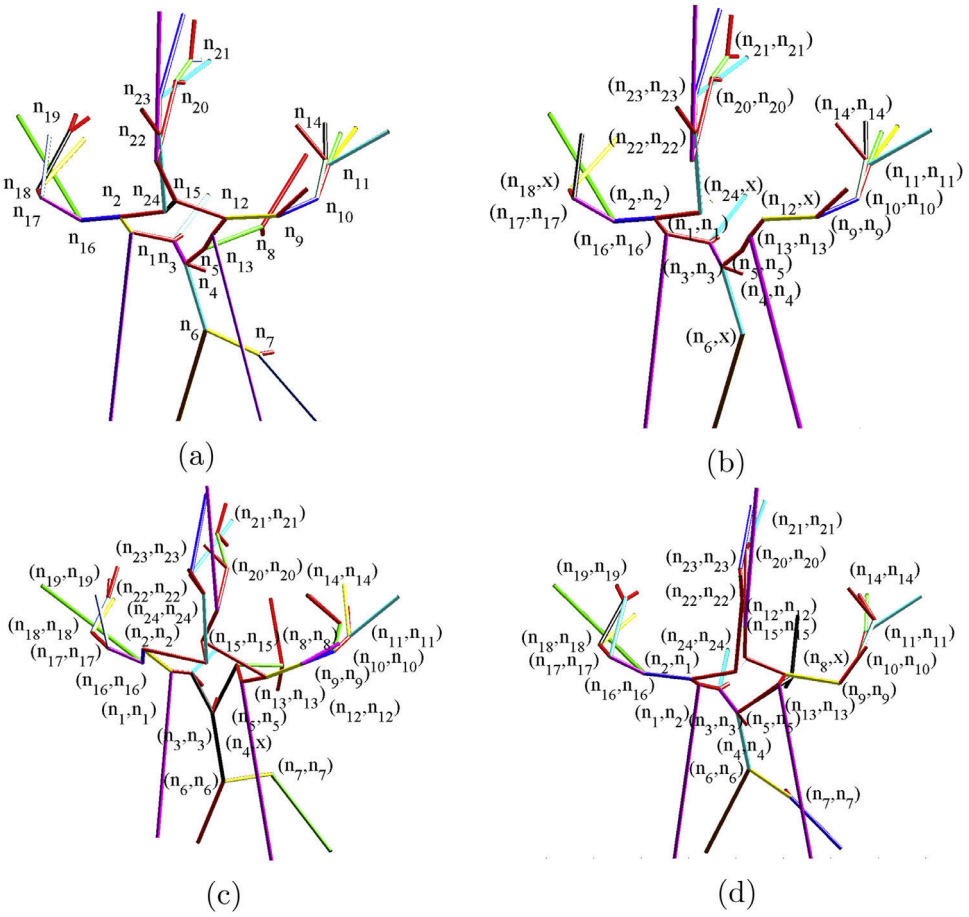


Fig. 10. (a) A base MRA-driven abstract graph and its synthetic modification with (b) $\alpha = 0.18, \sigma_\eta = 0$, and $\lambda = 10$, (c) $\alpha = 0, \sigma_\eta = 10$, and $\lambda = 10$, and (d) $\alpha = 0, \sigma_\eta = 5$, and $\lambda = 50$. The node labels reflect the ground truth (left) and the label of the node that they are matched to (right) this replaces with a cross sign for unmatched nodes. Matched edges are similarly colored in the same hues where un-matched edges are presented in black.

in the context of real-world structural discrepancies and abnormalities. The results are provided for total of a 171 cases including 105 pair-wise matchings obtained from fifteen MRA images (nine healthy samples and six samples from patients with aneurysm) and 66 pair-wise matchings obtained from twelve healthy 3DRA datasets. The ground truth is determined via expert's comparative investigation with the original gray-scale angiography images. Fig. 11 shows the qualitative outcome of the registration for two MRA images and GGMs derived from them. The node correspondences between the abstract graphs found by the proposed method are marked with red double-headed arrows.

The *TPR, PPV*, and *FPR* measures are provided in Figs. 12(a) and (b) for nodes and edges respectively. The sensitivity of node matching is seen to be more affected by the structural variations where its average is around 86% and precision is 88%. The edge matching sensitivity is around 84% on average where the average of precision falls around 86%. The higher *PPV* is due to the relatively lower number of false positives rather than the false negatives. Also, the number of edge matchings decreases with a higher rate than nodes as they are dependent on four nodes to be matched. The average *FPR* is around $5-7\%$ where its standard deviation demonstrates to stay lower compared to *TPR* and *PPV* in the plots. This characteristic is of high value in clinical settings where wrong correspondences could misguide diagnosis or prognosis with more impact.

We have examined the efficiency of signature design vs. the case that nodes are matched with costs calculated solely based on their geometrical attributes such that Q_{ij}^{A} in (6) is calculated as $\|\phi_2(v_j) - \phi_1(v_i)\|_F - \lambda$. For this purpose, graphs derived from MRA and 3DRA datasets are separately matched and average accuracy defined as

$$\frac{\text{True positives} + \text{True negatives}}{\text{Problem size}} \tag{12}$$

are measured and presented in Fig. 13. These results confirm that inclusion of local topological information in the form of signatures (red bars) indeed improves the performance by at least 20% for the two given datasets.

Multi-modal matching: Due to invasiveness of some imaging procedures that is the case with 3DRA which calls for contrast agent injection, it is of great importance to develop methods capable of multimodal matching to avoid the difficulties given images of other modalities. To prove our algorithm's capacity in this respect where there is a larger difference between n_1 and n_2 in addition to the node displacements, we consider its application to pairs of graphs derived from MRA and 3DRA images. Because 3DRA data is collected over only half of the cerebrovasculature, the MRA data is likewise divided. Compared to MRA-only matchings, the *TPR* or sensitivity has increased due to the higher amount of structural details present in 3DRA images. For the same reason, there is larger number of false positives that slightly reduces the *PPV* and increases the *FPR*s. The node and edge related *TPR, PPV*, and *FPR* that are obtained from matching 25 pairs of graphs (5 from MRA and 5 from 3DRA data) are presented in the plots of Figs. 14(a) and (b). The *TPR, PPV*, and *FPR* for node matchings are around 84%, 83%, and 8% respectively. The edge matching performs with a slightly lower accuracy than the node matching, *TPR* is 83% and average *PPV* is 86% where *FPR* reduces to 5%. These values are comparable

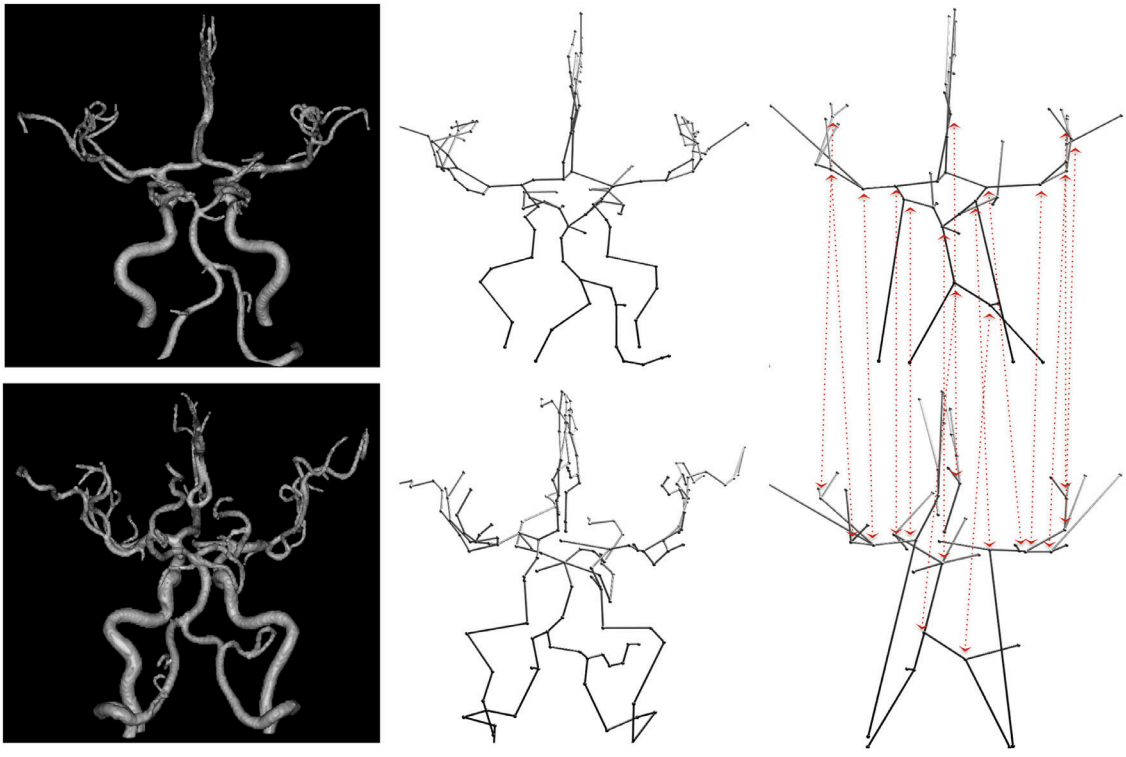


Fig. 11. Left to right: Two segmented MRA datasets, their GGMs, and abstract graphs. The obtained node correspondences are demonstrated with red arrows. (For interpretation of the references to color in this figure legend, the reader is referred to the web version of this article.)

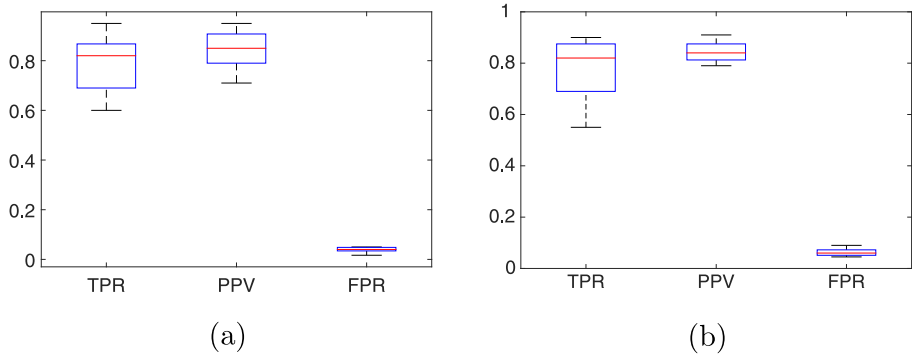


Fig. 12. Measures of *TPR*, *PPV*, and *FPR* for (a) nodes and (b) edges matching results obtained from 171 cases including 105 pair-wise matchings of 15 graphs obtained from MRA images and 66 pair-wise matchings of twelve graphs modeling 3DRA datasets.

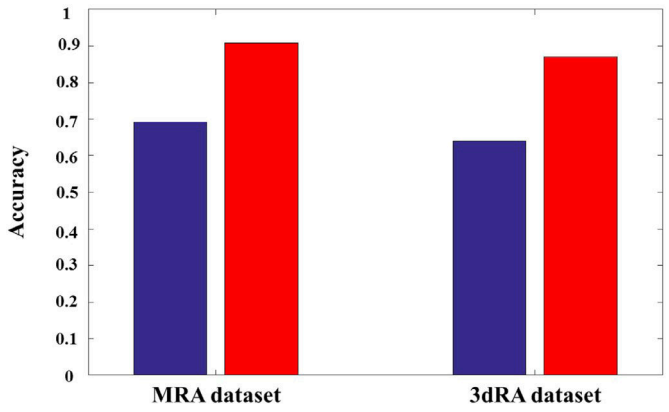


Fig. 13. Average matching accuracy measure for nodes across MRA and 3DRA datasets using geometrical (blue) and combined geometrical and topological (red) properties of the abstract graphs. (For interpretation of the references to color in this figure legend, the reader is referred to the web version of this article.)

to the mono-modal matching results that confirm the efficiency of GMR in multi-modal matching.

Fig. 15 shows the results of testing the performance across different node levels. The method performs better at the lower levels where aneurysm is typically found (Wiebers, 2003). However, the performance variation across levels is not significant that makes the algorithm efficient for pathologies that affect deeper levels as well like non-aneurysmal stroke.

3.5.3. Comparative evaluation of GMR

To demonstrate that how the overall graph matching performance is enhanced by GMR, we have analyzed its performance versus the state-of-the-art graph matching methods: HGM (Zass and Shashua., 2008), SMAC (Cour et al., 2007), MWC ((Ma and Latecki, 2012, Czajkowska et al., 2015), and RRWM (Cho et al., 2010) in terms of node matching accuracy (specifically TPR vs. FPR) and running time. These methods solve the (3) given the unary and pair-wise node correspondence costs (c_{ij} and $d_{iji'j'}$). We have set these costs to be $\|\phi_2(v_j) - \phi_1(v_i)\|_F$ and $\|\zeta_2(v_j, v_b) - \zeta_1(v_i, v_a)\|_F$

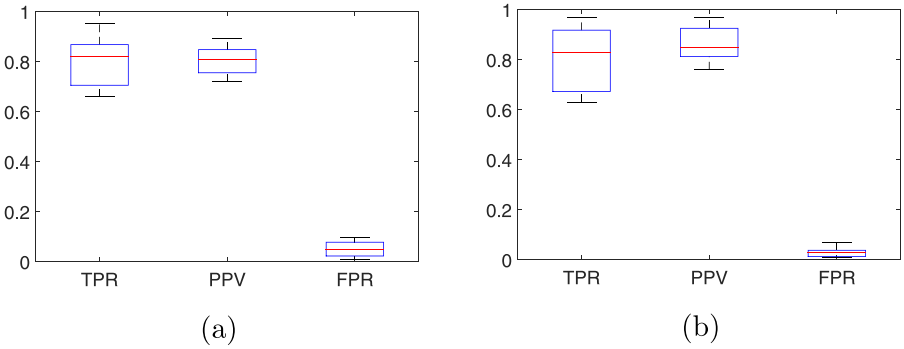


Fig. 14. Measures of *TPR*, *PPV*, and *FPR* for (a) nodes and (b) edges matching results of graphs derived from fifteen MRA and twelve 3DRA images.

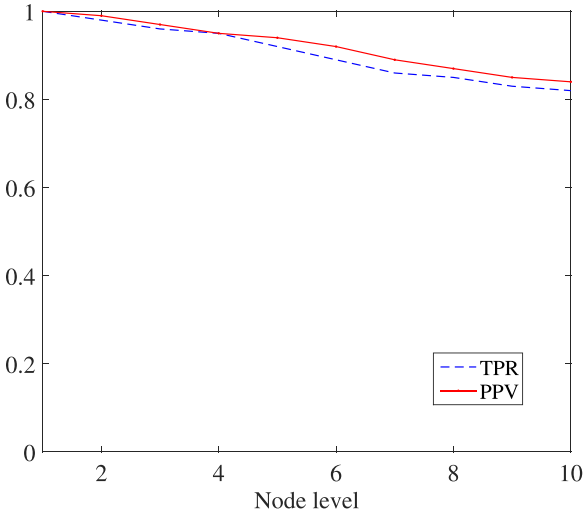


Fig. 15. The average *TPR* and *PPV* values for different node levels.

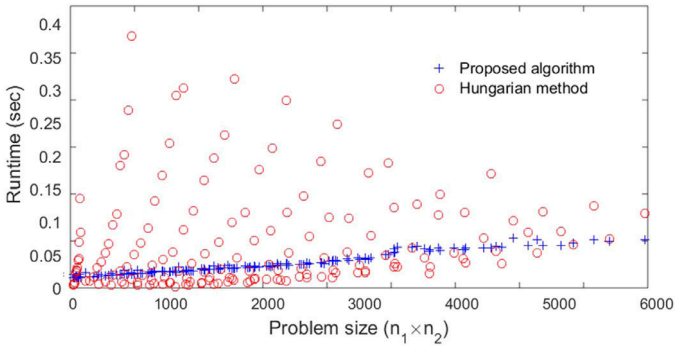


Fig. 17. Runtime of the GA-based method (blue crosses) vs. Hungarian matching (red circles). (For interpretation of the references to color in this figure legend, the reader is referred to the web version of this article.)

where v_1, $v_a \in V_1$ and v_2, $v_b \in V_2$. The costs are calculated for the synthetic graphs used in Section 3.5.1 and clinical (healthy and unhealthy) data derived graphs of Section 3.5.2 have collectively been matched to show the stability of method against a wide variety of synthetic and pathological variations.

HGM, SMAC, and RRWM are run using their publicly available MATLAB codes. The MWC algorithms has been implemented in MATLAB based on the algorithm presented in (Ma and Latecki, 2012). The parameters are tuned such that the highest TPR is delivered by average for all of the methods on our datasets. For MWC, $\epsilon = 0.01$, and for RRWM, the reweigh factor $\alpha = 0.2$ and inflation factor $\beta = 30$. These values comply with the ones recommended in the respective papers.

Fig. 16(a) demonstrates the accuracy results. The node correspondence TPR vs. FPR curve is plotted in green for our approach, GMR and shows a higher precision relative to the other methods. The SMAC (in blue), MWC (in red), HGM (in yellow), and RRWM (in purple) methods come next in the performance. To compare the methods in terms of speed, the running time is measured as a function of total problem size $n_t = n_1 \times n_2$. For the synthetic and

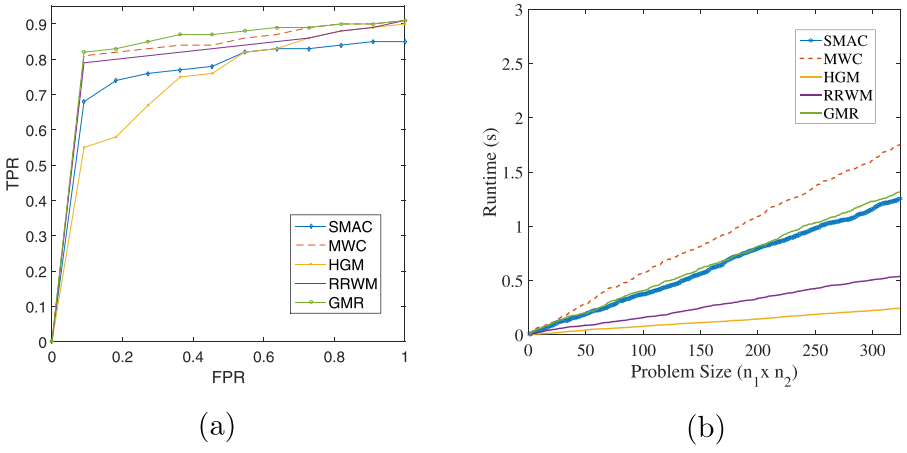


Fig. 16. The ROC curve (Left) and runtime (right) results are plotted for SMAC (blue), MWC (red), HGM (yellow), RRWM (purple), and GMR (green). (For interpretation of the references to color in this figure legend, the reader is referred to the web version of this article.)

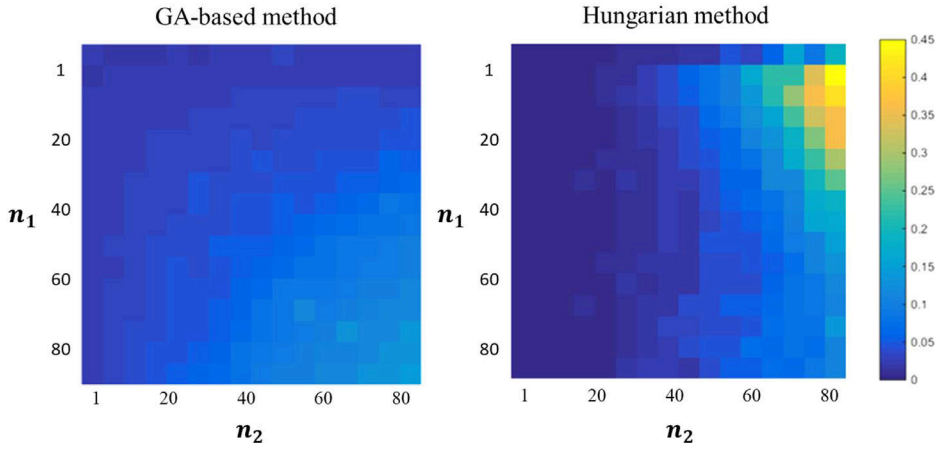


Fig. 18. Heat maps of the GA-based and Hungarian methods running time vs. the sets cardinalities n_1 and n_2.

clinical data sets used here n_i was between 1 and 354. The experiments were performed on a 3.0 GHz CPU and 32.00 GB RAM platform. According to Fig. 16(b), GMR is faster than MWC and runs at approximately the same speed as SMAC approach. The HGM method has the highest speed for the problem size range. However, it is also the least accurate. RRWM also is faster than GMR, but as with HGM, is less accurate than the approach we have developed. Considering both metrics, our approach is marginally more accurate and substantially less costly as the size of the problem increases.

More specifically, in an analysis prompted by a Reviewer, we compared running time of the GA-based binary assignment and augmented Hungarian method for problem sizes of 1 to 6400 produced according to the Section 3.5.1. The runtime of the GA is measured for parameters β_0, β_r, β_f, $I_{\max}$, and ϵ tuned as described in the Section 3.3 that yield exactly the same matching accuracy as the Hungarian algorithm. For this purpose, the Hungarian method has to be adapted to the null match case by building a $(n_1+n_2)\times(n_1+n_2)$ assignment matrix whose last n_1 columns and n_2 rows are zero. The results in Fig. 17 show a linear increase in timing for the GA method from about 0.025 s to 0.143 s. The Hungarian method on the other hand demonstrates rather large variability (0.001 to 0.449 s) depending much more on the specific sizes of the two graphs. Specifically, another demonstration of these data in Fig. 18 suggests that, for problems where there is a large imbalance in node sizes, the runtime of the Hungarian method becomes quite large. In more balanced cases, the GA is a bit slower. Motivated by the stability of the GA-based method, we have chosen to employ this technique as the basis of analysis in this work.

4. Conclusion

Relative to the common registration methods, either intensity or feature-based techniques, use of topological information can dramatically enhance the robustness to imaging and image processing artifacts and inter-sample variations by regularizing the problem with information about the shape of the objects. Exploiting this fact, we presented a landmark-based registration method for GGMs. The GGMs display different node counts and edge distortions giving rise to an inexact graph matching problem that is usually approached by solving an NP-hard quadratic assignment problem. We have tackled the computational complexity dilemma by transforming the QAP into a point correspondence problem where point sets here, represent the bifurcations. For this reason, the registration has been achieved in three steps. First, GGMs are brought to a roughly similar global alignment, scale, and placement. Next, we introduced a novel node signature considering the major structural specifications of vessels that also comply with the features correlated to the aneurysm formation. They incorporate the geometric attributes and the local topological information. The point correspondence is posed as a linear assignment problem and solved using a proposed variation of the graduated assignment technique. Finally, the edges are registered through a heuristic method.

The method's performance has been tested on a collection of clinical angiography images and synthetic datasets. Quantitative results in the form of sensitivity and precision of matched nodes and edges, suggest that this method is highly reliable under the influence of different types of perturbation including node displacement and problem size. Quality of inter-subject and multimodal matching of clinical data have also been confirmed.

One area of future work would be to increase the method's capacity by adding flexibility to the number of connections in the signature definition. If the proposed registration method were generalized to allow for an arbitrary number of connections, it will be applicable to any vasculature or tubular network in biological subjects. Also, establishing a method for automated determination of λ would benefit the overall performance. Testing the method on graphs showing more inclusive kinds of pathological perturbations falls in the future scope of the work that requires adaptation of geometrical features in the signature definition.

Given such an efficient registration method, one can use the universality of the graphs, which is their independence from modalities, to devise strong and effective statistical analysis frameworks for anomaly detection and prognosis. Graphs also provide a relatively low dimensional representation that is a major advantage for applications involving large-scale datasets. The correspondences found by this approach can also be used as a blueprint for a full intensity-based registration.

References

Agostoni, E.C., Longoni, M., 2015. Cerebrovascular interactions in cerebral disorders (stroke, transient ischaemic attacks, microvascular disease, migraine). In: Arterial Disorders. Springer International Publishing, pp. 333–345.

Almasi, S., Xu, X., Ben-Zvi, A., Lacoste, B., Gu, C., Miller, E.L., 2015. A novel method for identifying a graph-based representation of 3-D microvascular networks from fluorescence microscopy image stacks. Med. Image Anal. Vol. 20, 208–223.

Amin-Hanjani, S., Du, X., Pandey, D.K., Thulborn, K.R., Charbel, F.T., 2015. Effect of age and vascular anatomy on blood flow in major cerebral vessels. J. Cereb. Blood Flow Metabol. 35 (2), 312–318.

Baharoglu, M.I., Lauric, A., Safain, M.G., Hippelheuser, J., Wu, C., Malek, A.M., 2014. Widening and high inclination of the middle cerebral artery bifurcation are associated with presence of aneurysms. Stroke 45 (9), 2649–2655.

Bai, X., Latecki, L.J., 2008. Path similarity skeleton graph matching, pattern analysis and machine intelligence. Trans. IEEE 30 (7), 1282–1292.

Benseghir, T., Malandain, G., Vaillant, R., 2015. A tree-topology preserving pairing for 3d/2d registration. Int. J. Comput. Assist. Radiol. Surg. 10 (6), 1–11.
Burkard, R.E., 2013. Quadratic Assignment Problems. Springer, New York, pp. 2741–2814.
Cho, M., Jungmin, L., Kyoung, M.L., 2010. Reweighted random walks for graph matching. In: Computer Vision, ECCV. Springer Berlin Heidelberg, pp. 492–505.
Chui, H., Rangarajan, A., 2003. A new point matching algorithm for non-rigid registration. Comput. Vis. Image Underst. 89 (2), 114–141.
Conte, D., Foggia, P., Sansone, C., Vento, M., 2004. Thirty years of graph matching in pattern recognition. Int. J. Pattern Recognit. Artif. Intell. 18, 265–298.
Cour, T., Srinivasan, P., Shi, J., 2007. Balanced graph matching. Adv. Neural Inf. Process. Syst. 19 (313). https://www.nlm.nih.gov/medlineplus/ency/imagepages/18009.htm.
Czajkowska, J., Feinen, C., Grzegorzek, M., Raspe, M., Wickenhöfer, R., 2015. Skeleton graph matching vs. maximum weight cliques aorta registration techniques. Comput. Med. Imaging Graph 46, 142–152.
Gold, S., Rangarajan, A., 1996. A graduated assignment algorithm for graph matching. IEEE Trans. Pattern Anal. Mach. Intell. 18 (4), 377–388.
Gold, S., Rangarajan, A., Lu, C.P., Pappu, S., Mjolsness, E., 1998. New algorithms for 2d and 3d point matching: pose estimation and correspondence. Pattern Recognit. 31 (8), 1019–1031.
Gori, M., Maggini, M., Sarti, L., 2005. Exact and approximate graph matching using random walks. IEEE Trans. Pattern Anal. Mach. Intell. 27 (7), 1100–1111.
Horn, R.A., Johnson, C.R., 2012. Matrix Analysis. Cambridge university press.
Hu, N., Rustamov, R.M., Guibas, L., 2013. Graph matching with anchor nodes: a learning approach. In: Proceedings of the IEEE Conference on Computer Vision and Pattern Recognition, pp. 2906–2913.
Ingebrigtsen, T., Morgan, M.K., Faulder, K., Ingebrigtsen, L., Sparr, T., Schirmer, H., 2004. Bifurcation geometry and the presence of cerebral artery aneurysms. J. Neurosurg. 101 (1), 108–113.
Jouili, S., Tabbone, S., 2009. Graph matching based on node signatures. In: Proceedings of the International Workshop on Graph-Based Representations in Pattern Recognition. Springer Berlin, Heidelberg, pp. 154–163.
Lauric, A., Safain, M.G., Hippelheuser, J., Malek, A.M., 2014. High curvature of the internal carotid artery is associated with the presence of intracranial aneurysms. J. Neurointerv. Surg. 6 (10), 733–739.
Leordeanu, M., Hebert, M., 2005. A spectral technique for correspondence problems using pairwise constraints. IEEE Int. Conf. Comput. Vis. (ICCV) 2, 1482–1489.
Leordeanu, M., Hebert, M., Sukthankar, R., 2009. An integer projected fixed point method for graph matching and map inference. In: Advances in neural information processing systems, pp. 1114–1122.
Leordeanu, M., Sukthankar, R., Hebert, M., 2012. Unsupervised learning for graph matching. Int. J. Comput. Vis. 96 (1), 28–45.
Metzen, J.H., Kroger, T., Schenk, A., Zidowitz, S., Peitgen, H.O., Jiang, X., 2009. Matching of anatomical tree structures for registration of medical images. Image Vis. Comput. 27 (7), 923–933.
Mitrovic, U., Spiclin, Z., Likar, B., Pernus, F., 2013. 3D-2d registration of cerebral angiograms: a method and evaluation on clinical images. IEEE Trans. Med. Imaging 32 (8), 1550–1563.
Rangarajan, A., Chui, H., Bookstein, F.L., 1997. The softassign procrustes matching algorithm. In: Information Processing in Medical Imaging. Springer, Berlin Heidelberg, pp. 29–42.
Salmon, J.P., Debled-Rennesson, I., Wendling, L., 2006. A new method to detect arcs and segments from curvature profiles. In: Proceedings of the International Conference on Pattern Recognition, ICPR (3) 387–390.
Schellewald, C., Roth, S., Schnrr, C., 2007. Evaluation of a convex relaxation to a quadratic assignment matching approach for relational object views. Image Vis. Comput. 25 (8), 1301–1314.
Sebastian, T.B., Kimia, B.B., 2005. Curves vs. skeletons in object recognition. Signal Process. 85 (2), 247–263.
Serradell, E., Pinheiro, M.A., Sznitman, R., Kybic, J., Moreno-Noguer, F., Fua, P., 2015. Non-rigid graph registration using active testing search. IEEE Trans. Pattern Anal. Mach. Intell. 37 (3), 625–638.
Siddiqi, K., Shokoufandeh, A., Dickinson, S.J., Zucker, S.W., 1999. Shock graphs and shape matching. Int. J. Comput. Vis. 35 (1), 13–32.
Sinkhorn, R., 1964. A relationship between arbitrary positive matrices and doubly stochastic matrices. Ann. Math. Stat. 876–879.
Smeets, D., Bruyninckx, P., Keustermans, J., Vandermeulen, D., Suetens, P., 2010. Robust matching of 3d lung vessel trees. In: Proceedings of the MICCAI Workshop on Pulmonary Image Analysis.
Sonka, M., Hlavac, V., Boyle, R., 1993. Image Processing, Analysis and Machine Vision. Springer, New York.
Tutuncu, F., Schimansky, S., Baharoglu, M.I., Gao, B., Calnan, D., Hippelheuser, J., Safain, M.G., Lauric, A., Malek, A.M., 2014. Widening of the basilar bifurcation angle: association with presence of intracranial aneurysm, age, and female sex. Clin. Article. J. Neurosurg. 121 (6), 1401–1410.
Wiebers, D.O., 2003. International study of unruptured intracranial aneurysms investigators, unruptured intracranial aneurysms: natural history, clinical outcome, and risks of surgical and endovascular treatment. The Lancet 362 (9378), 103–110.
Wong, P.C., Foote, H., Chin, G., Mackey, P., Perrine, K., 2006. Graph signatures for visual analytics. IEEE Trans. Vis. Comput. Graph. 12 (6), 1399–1413.
Yan, J., Wang, J., Zha, H., Yang, X., Chu, S., 2015. Consistency-driven alternating optimization for multigraph matching: A unified approach. IEEE Trans. Image Process. 24 (3), 994–1009.
Zaslavskiy, M., Bach, F., Vert, J.P., 2009. A path following algorithm for the graph matching problem. IEEE Trans. Pattern Anal. Mach. Intell. 31 (12), 2227–2242.
Zass, R., Shashua., A., 2008. Probabilistic graph and hypergraph matching. IEEE Conference on Computer Vision and Pattern Recognition (CVPR) 1–8.
Zhu, Y., Qin, L., Yu, J.X., Ke, Y., Lin, X., 2013. High efficiency and quality: large graphs matching. VLDB J. 22 (3), 345–368.